

# Atmospheric Carbon Dioxide Measurement from Aircraft and Comparison with OCO-2 and CarbonTracker Model Data

Qin Wang<sup>1</sup>, Farhan Mustafa<sup>1</sup>, Lingbing Bu<sup>1</sup>, Shouzheng Zhu<sup>1,2</sup>, Jiqiao Liu<sup>2</sup>, Weibiao Chen<sup>2</sup>

5 <sup>1</sup>Collaborative Innovation Center on Forecast and Evaluation of Meteorological Disasters, Nanjing University of Information Science and Technology (NUIST), Nanjing, 210044, China

<sup>2</sup>Key Laboratory of Space Laser Communication and Detection Technology, Shanghai Institute of Optics and Fine Mechanics, Chinese Academy of Sciences, Shanghai 201800, China

*Correspondence to:* Lingbing Bu (lingbingbu@nuist.edu.cn)

10 **Abstract.** Accurate monitoring of the atmospheric carbon dioxide (CO<sub>2</sub>) and its distribution is of great significance for studying the carbon cycle and predicting the future climate change. Compared to the ground observational sites, the airborne observations cover a wider area, and simultaneously observe a variety of surface types, which help in effectively monitoring the distribution of CO<sub>2</sub> sources and sinks. In this work, an airborne experiment was carried out in March 2019 over Shanhaiguan area, China (39N-41N,119E-121E). An Integrated Path Differential Absorption (IPDA) Light Detection and Ranging (LIDAR) system and a commercial instrument, the Ultraportable Greenhouse Gas Analyzer (UGGA), were used installed on an aircraft to observe the CO<sub>2</sub> distribution over various surface types. The Pulse Integration Method (PIM) algorithm was used to calculate the Differential Absorption Optical Depth (DAOD) from the LIDAR data. The CO<sub>2</sub> column-averaged dry-air mixing ratio (XCO<sub>2</sub>) was calculated over different types of surfaces including mountain, ocean and urban areas. The concentrations of the XCO<sub>2</sub> calculated from LIDAR measurements over ocean, mountain, and urban areas were  $421.11 \pm 1.24$  ppm,  $427.67 \pm 0.58$  ppm, and  $432.04 \pm 0.74$  ppm, respectively. Moreover, through the detailed analysis of the data obtained from the UGGA, the influence of pollution levels on the CO<sub>2</sub> concentration was also studied. During the whole flight campaign, March 18 was heavily polluted with an Air Quality Index (AQI) of 175 and PM<sub>2.5</sub> of 131  $\mu\text{g}/\text{m}^3$ . The Aerosol Optical Depth (AOD) reported by a sun photometer installed at the Funning ground station was 1.28. Compared to the other days, the CO<sub>2</sub> concentration measured by UGGA at different heights was the largest on March 18 with an average value of  $422.59 \pm 6.39$  ppm, that was about 10 ppm higher than the measurements recorded on March 16. Moreover, the vertical profiles of Orbiting Carbon observatory-2 (OCO-2) and CarbonTracker were also compared with the aircraft measurements. All the datasets showed a similar variation with some differences in their CO<sub>2</sub> concentrations, which showing a good agreement among them.

## 1 Introduction

30 Atmospheric carbon dioxide (CO<sub>2</sub>) is the most important greenhouse gas, and it plays a significant role in hydrology, sea ice melting, sea level rise, and atmospheric temperature changes (Mustafa et al., 2020; Santer et al., 2013; Stocker et al., 2013).

Since the industrial revolution, the increase in the anthropogenic activities have caused a significant rise in the CO<sub>2</sub> concentration, which is considered an important factor for climate change (Ballantyne et al., 2012; Dlugokencky Ed, 2016). Accurate measurement of atmospheric CO<sub>2</sub> and its spatiotemporal variation is crucial for estimating the distribution and dynamics of carbon sources and sinks at regional and global scales (Araki et al., 2010; Mustafa et al., 2021). There are several ground-based stations such as the Total Carbon Column Observing Network (TCCON) sites and the stations within the Global Atmospheric Watch (GAW) network, which are monitoring the atmospheric CO<sub>2</sub> with great precision (Hedelius et al., 2017; Hungershofer et al., 2010; Mendonca et al., 2019; Schultz et al., 2015). However, these observational sites are not sufficient to accurately monitoring the atmospheric CO<sub>2</sub> at regional and global scales due to their limited spatial coverage and uneven distribution (Kulawik et al., 2016). Previous studies suggested that the space-based instruments could provide the most effective way to monitor the atmospheric CO<sub>2</sub> at regional and global scales with great spatiotemporal resolutions (Kong et al., 2019; Lindqvist et al., 2015). Since the past decade, several satellites have been launched which are dedicatedly monitoring the greenhouse gases including the atmospheric CO<sub>2</sub> and methane (Crisp, 2015; Yokota et al., 2009). These satellites calculate the average atmospheric CO<sub>2</sub> concentrations in the path of sunlight reflected by the surface through spectrometers carried onboard. The measurements obtained from these satellites are affected by clouds and aerosols and much of the data is screened out due to the contamination of clouds and aerosol content in the measurements. Greenhous gases Observing SATellite (GOSAT) and the Orbiting Carbon observatory-2 (OCO-2) were the first two CO<sub>2</sub> monitoring satellites which were successfully put into the orbit. Both of them measure the CO<sub>2</sub> optical depth with the bands centred around 1.6 μm and 2.0 μm, and O<sub>2</sub> with band A, centred around 0.76 μm (Kiel et al., 2019).

The Integrated Path Differential Absorption (IPDA) Light Detection and Ranging (LIDAR) is also an effective tool to observe the atmospheric CO<sub>2</sub> and other atmospheric variables (Gong et al., 2020; Xie et al., 2020; Zhu et al., 2020). Several studies have used the ground-based and airborne IPDA LIDAR systems to measure the atmospheric CO<sub>2</sub> (Ehret et al., 2008; Kawa et al., 2010). Moreover, the feasibility and the sensitivity analyses of the space-borne CO<sub>2</sub> monitoring LIDAR systems have also been carried out and the corresponding instruments have been put into use in several countries including the United States, China, and Germany (Abshire et al., 2013; Mao et al., 2018b, 2018a; Du et al., 2017; Liang et al., 2017; Amediek et al., 2017). Like the GOSAT and OCO-2, most of the IPDA LIDAR systems also focus on the wavelengths of 1.6 μm and 2.0 μm to measure the atmospheric CO<sub>2</sub>. The National Aeronautics and Space Administration (NASA) Goddard Space Flight centre developed a pulsed IPDA LIDAR instrument incorporating a HgCdTe Avalanche Photodiode detector (APD) and multiple-wavelength-locked laser to measure the CO<sub>2</sub> column-averaged dry-air mixing ratio (XCO<sub>2</sub>) and carried out its first airborne campaign in 2011 (Abshire et al., 2013). Later, the instrument was improved and the latest results from the airborne campaign carried out during 2014 and 2016 showed an accuracy of 0.8 ppm over a desert area (Abshire et al., 2018). The measurements obtained from the IPDA LIDAR system were evaluated against in-situ instrument observations and the differences were within a range of 1 ppm. Another CO<sub>2</sub> monitoring double-pulsed, 2 μm IPDA LIDAR instrument developed by NASA Langley Research Centre carried out its airborne operation in 2014 to measure the atmospheric CO<sub>2</sub> (Refaat et al., 2016). The results showed a difference of 0.36% relative to the CO<sub>2</sub> mixing ratio measured by the National Oceanic and Atmospheric

65 Administration (NOAA) flask sampling data (Yu et al., 2017). In addition, the German Aerospace Center (DLR) developed a 1.57  $\mu\text{m}$  double-pulse IPDA LIDAR instrument and measured the atmospheric  $\text{CO}_2$  concentration with great accuracy during their airborne campaign in 2015 (Amediek et al., 2017).

China significantly contributes to the global  $\text{CO}_2$  emission mainly due to the strong anthropogenic activities (Mustafa et al., 2020). The northern China, in particular, Beijing-Tianjin-Hebei is the most populated region with the largest anthropogenic  
70 emissions in the world (Lei et al., 2017; Yang et al., 2019). Under the United Nations Framework Convention on Climate Change (UNFCCC) 2015 Paris Climate Agreement, China pledged to reduce the  $\text{CO}_2$  emission per unit gross domestic product (GDP) by 60-65% compared to 2005 levels, and peak carbon emission overall, by 2030 (UNFCCC, 2015). It is crucial to measure the atmospheric  $\text{CO}_2$  using precise and accurate instruments for monitoring of the  $\text{CO}_2$  reduction progress and evaluation of how well specific policies are working. In this study, an airborne campaign was carried out during March 2019 to measure the  
75 atmospheric  $\text{CO}_2$  using an IPDA LIDAR, and a commercial instrument Ultraportable Greenhouse Gas Analyzer (UGGA; model 915-0011; Los Gatos Research, San Jose, CA, USA) over northeast China. The primary objective of the study was to evaluate the performance of a newly developed IPDA LIDAR instrument over different types of surfaces including water bodies, mountains and urban residential areas. In addition, the influence of pollution on the atmospheric  $\text{CO}_2$  concentration was also studied using the measurement obtained from the UGGA installed on the aircraft. The details about observational  
80 site, flight campaign, and instruments are provided in Section 2. The results including the IPDA LIDAR measurements, UGGA observations and their comparisons are discussed in Section 3. And our conclusions are presented in Section 4.

## 2 Materials and Methods

The northern China, in particular, Beijing-Tianjin-Hebei is the most populated region with the largest anthropogenic emissions in the world. Several studies reported larger uncertainties in the satellite  $\text{CO}_2$  retrievals over North and East China (Sun et al.,  
85 2020). Therefore, the accurate measurement of  $\text{CO}_2$  in the atmosphere is of great significance. Moreover, validation of model measurements against accurate  $\text{CO}_2$  profiles is also crucial, because the satellite retrieval algorithms require a priori profiles which are generally based on models and in situ data. CarbonTracker is one of model widely used by the  $\text{CO}_2$  community and IPDA lidar is an effective tool for high-precision observation of atmospheric  $\text{CO}_2$ .

### 2.1 Aircraft Instrumentation

90 The aircraft used in this experiment was a Yun-8, which was equipped with four turboprop engines. The cruise and the maximum speeds of the aircraft were 550  $\text{km h}^{-1}$  and 660  $\text{km h}^{-1}$ , respectively. The Atmospheric Carbon Dioxide LIDAR (ACDL) conducted its first flight experiment during March 2019 over Shanhaiguan, China. The working wavelengths of the ACDL were 532 nm, 1064 nm, and 1572 nm, respectively. The 1572 nm channel was used for IPDA technique to measure the atmospheric  $\text{CO}_2$ , while the 532 nm and 1064 nm channels were used to detect aerosols and clouds. The aerosol and cloud  
95 optical parameters, such as the extinction coefficient, backscatter coefficient, LIDAR ratio and the Aerosol Optical Depth (AOD) are helpful in providing accurate inversion of  $\text{CO}_2$  column concentration (Crisp et al., 2012; O'Dell et al., 2012). More

detail about the ACDL is described in (Zhu et al., 2020). The ACDL system used for the atmospheric CO<sub>2</sub> measurement is shown in Figure 1, and more detail about the main components of the system is provided in Table 1.

**Table 1: The main parameters of the airborne dual-wavelength IPDA LIDAR system.**

Parameters	Value	Parameters	Value
Online wavelength	1572.024 nm	Telescope diameter	150 mm
Offline wavelength	1572.085 nm	Field of view	1 mrad
Pulse energy(on/off)	6/3 mJ	Beam divergence	0.62 mrad
Pulse width(on/off)	17 ns	Emission optical efficiency	0.8955
Repetition frequency	30 Hz	Receiver optical efficiency	0.3797
Frequency stability	2.7 MHz	Data acquisition	125 MS/s
Pulse spectral linewidth (OPA)	30 MHz		

The ACDL consisted of a laser transmitter, an instrument control, an environmental control, and a LIDAR transceiver subsystem. Figure 1(a) shows the transceiver system. It mainly included a laser, a telescope, a receiving system and an APD detector, which were mounted in a pod outside the aircraft. Figure 1(b) shows the laser frequency monitoring and control system, electronic control system and the data acquisition system of the equipment. These systems were installed inside the aircraft and armoured optical fibres and cables were used to transmit the information to the instruments in the pod. An Inertial Navigation System (INS) was also installed to record the attitude information of the aircraft during the flight. The real-time altitude and position information of aircraft were acquired using a Global Positioning System (GPS) system. Figure 1(c) shows the Aircraft Integrated Meteorological Measurement System (AIMMS). The AIMMS was installed to measure the atmospheric temperature, pressure, relative humidity and other meteorological parameters during the flight. Figure 1(d) shows a commercial instrument UGGA, that was installed in an unsealed cabin of the aircraft and a 1/4-inch Teflon pipe was used to connect it with the external atmosphere. The UGGA used a laser absorption technology known as the off-axis Integrated Cavity Output Spectroscopy (ICOS) to measure trace gas concentration in dry mole fraction with a high precision of <0.30 ppm for CO<sub>2</sub> and <2 ppb for CH<sub>4</sub> (UGGA user manual; model 915-0011; Los Gatos Research, San Jose, CA, USA). More details about the UGGA and ICOS spectroscopy are given in previous studies (Baer et al., 2002; Paul et al., 2001; Sun et al., 2020). Before the flight experiment, the UGGA was calibrated against the standard gas, and the uncertainty was within 0.1 ppm.

## 2.2 Experimental Site

The airborne campaign was conducted from 11 – 19 March 2019. More detail about the flights is given in Table 2. Figure 2 shows the geolocation of the experimental site and path of the flight carried out on 14 March. In order to detect the changing trend of atmospheric CO<sub>2</sub> concentration over various types of surfaces, the path of the flight was designed to observe the ocean, urban residential and the mountain areas. The starting point of the flight was A, and the ending point was B. The flight path covered a variety of surface types, including the ocean, the mountain, and the urban residential areas. The distribution of the carbon sources and sinks in the study area can be more accurately distinguished through the detection of various surface types.

Figure 3 shows the flight altitude and the corresponding surface elevation information during the level flight period. The altitude of the aircraft was measured by the GPS system. The height and the ground elevation were measured using the airborne IPDA LIDAR. The altitude of the horizontal flight of the plane on March 14 was about 6.8 km. Moreover, the altitude information about various types of surfaces is also shown in Figure 3.

**Table 2: Details of flight on each day.**

<b>Date</b>	<b>Horizontal flight time</b>	<b>Flight Altitude (km)</b>
11 March	10:26 - 14:43	5
14 March	10:18 - 12:06	6.8
16 March	10:34 - 12:46	7.8
18 March	10:21 - 14:18	4
19 March	10:21 - 14:05	5

## 130 2.3 Datasets

### 2.3.1 Aircraft Data

A variety of data were measured using the aircraft and incorporated in this study. The aircraft data included the ACDL data, in-situ data and the auxiliary data. The in-situ CO<sub>2</sub> dry-air mole fraction data was measured using the UGGA which was installed in an unsealed cabin of the aircraft. The auxiliary data included the inertial navigational and meteorological data. The inertial navigational data was measured using the INS, and the meteorological data was measured using the AIMMS, which was installed on the aircraft shell. In addition, a colour Complementary Metal Oxide Semiconductor (CMOS) camera (model: IDS ui-3360cp-c-hq Rev.2) with a resolution of 2048x1088 pixels was also installed next to the lidar telescope to observe the various types of surfaces. The image sampling rate was 1 Hz. Each picture incorporated the shooting time, and it provided a convenience to find the types of surfaces at different times. The photo name included the camera date and time, which was synchronized with the other instruments installed on the aircraft.

### 2.3.2 OCO-2 Dataset

The Orbiting Carbon observatory-2 (OCO-2), developed by NASA is the second satellite after the Greenhouse gases Observing SATellite (GOSAT) to monitoring the CO<sub>2</sub> in the atmosphere to get a better understanding of the carbon cycle (Crisp, 2015; Crisp et al., 2008). The main objectives of the mission included measuring the atmospheric CO<sub>2</sub> with sufficient precision, accuracy and spatiotemporal resolution required to quantify the CO<sub>2</sub> sources and sinks at regional and global scales. The sun-synchronous near-polar satellite included three high-resolution spectrometers simultaneously measuring of the reflected sunlight in the near-infrared CO<sub>2</sub> at 1.61  $\mu\text{m}$  and 2.06  $\mu\text{m}$  and oxygen at 0.76  $\mu\text{m}$  (Wunch et al., 2017). In this study, OCO-2 XCO<sub>2</sub> version 10r Level 2 Lite product was used.

### 2.3.3 CarbonTracker Dataset

150 Validation of model measurements against accurate CO<sub>2</sub> profiles is also crucial, because the satellite retrieval algorithms require a priori profiles which are generally based on models and in situ data. CarbonTracker is one of model widely used by the CO<sub>2</sub> community and IPDA lidar is an effective tool for high-precision observation of atmospheric CO<sub>2</sub>. In addition, the measurement range of passive remote sensing is limited, and the model can simulate the situation in a large range. CarbonTracker is an inverse model framework developed by (Peters et al., 2004). It combines the two-way nested transfer  
 155 model 5 (TM5) with offline Atmospheric Tracer transfer model and updates the atmospheric CO<sub>2</sub> distribution and surface fluxes every year (Krol et al., 2005). It supports high-resolution data at regional level and coarse-resolution data at global scale. The Carbon Tracker provides the global CO<sub>2</sub> distribution at 25 pressure levels with a spatial grid resolution of 3°×2° (Longitude/Latitude) and a temporal resolution of 3 hours (Babenhauserheide et al., 2015). The data product CTNRT2020 was used in this study (Jacobson et al., 2020).

### 160 2.4 IPDA Theory

The ACDL system developed for this study was based on two different wavelengths referred as the online and the offline wavelengths. The laser pulse of the online wavelength was strongly attenuated because it was absorbed by the CO<sub>2</sub> molecules while propagating through the atmosphere. In contrast, the offline pulse was only weakly attenuated (Zhang et al., 2020). The online and offline wavelengths selected in this study were not affected by other molecules than CO<sub>2</sub>. Because the online and  
 165 the offline wavelengths were very close, the difference of scattering and absorption caused by the aerosols and the gas molecules in the atmosphere could be ignored. Therefore, the difference between the two wavelength echo signals was mainly caused by atmospheric CO<sub>2</sub>. The airborne IPDA lidar equation (Ehret et al., 2008; Refaat et al., 2016) is given in the following:

$$P_e(\lambda, R_A) = \eta_r \cdot O_r \frac{A}{(R_A - R_G)^2} \cdot \frac{E(\lambda)}{\Delta t(\lambda)} \cdot \rho^* \cdot T_m \cdot \exp[-\tau_{CO_2}(\lambda, R_A)], \quad (1)$$

where  $P_e$  is the echo power,  $\lambda$  is the wavelength,  $\eta_r$  is the receiving optical efficiency,  $O_r$  is the overlap factor,  $A$  is the area  
 170 of the telescope,  $R_G$  is the height of the surface above sea level,  $R_A$  is the altitude of the aircraft platform,  $E$  is the emission energy of the laser,  $\Delta t$  is the effective pulse width of the echo pulse,  $\rho^*$  is the target reflectivity,  $\tau_{CO_2}$  is the two-way integral optical depth caused by CO<sub>2</sub> (given by Eq. (2) below), and  $T_m$  is the atmospheric transmission efficiency. The monitor signals of online and offline pulses are defined as  $P_0(\lambda_{on})$  and  $P_0(\lambda_{off})$ , respectively. The echo signals of the online and offline pulses are  $P(\lambda_{on}, R)$ , and  $P(\lambda_{off}, R)$ , respectively. The IPDA single-pass Differential Absorption Optical Depth (DAOD) of  
 175 the CO<sub>2</sub>,  $\tau_{CO_2}$ , can be expressed as (Refaat et al., 2015):

$$\tau_{CO_2} = \int_{R_G}^{R_A} \Delta\sigma_{CO_2}(p(r), T(r)) N_{CO_2}(r) dr = \frac{1}{2} \cdot \ln \left( \frac{P(\lambda_{off}, R) \cdot P_0(\lambda_{on})}{P(\lambda_{on}, R) \cdot P_0(\lambda_{off})} \right), \quad (2)$$

where  $\Delta\sigma_{CO_2}$  is the differential absorption cross section of the online and offline wavelengths,  $N_{CO_2}$  is the molecular density of the  $CO_2$ .  $p$  and  $T$  are pressure and temperature profiles. When the APD detector receives the signal, it can convert the power into voltage according to equation 3 (Zhu et al., 2020):

$$180 \quad V = P_p * \mathfrak{R}_v, \quad (3)$$

where  $\mathfrak{R}_v$ (V/W) represents the voltage response rate of the APD detector,  $P_p$  is the power of echo signal,  $V$  is the voltage. Within the linear response range of the detector, the voltage response rate is a fixed value  $\mathfrak{R}_v$  which indicates signal power. Using Eq. (3), equation 2 can also be expressed as:

$$\tau_{CO_2} = \frac{1}{2} \cdot \ln \left( \frac{V(\lambda_{off}, R) \cdot V_0(\lambda_{on})}{V(\lambda_{on}, R) \cdot V_0(\lambda_{off})} \right) \quad (4)$$

185 where  $V_0(\lambda_{on})$  and  $V_0(\lambda_{off})$  are the monitor signal voltages of online and offline pulses.  $V(\lambda_{on}, R)$  and  $V(\lambda_{off}, R)$  are the echo signal voltages of the online and offline pulses. For the airborne experiment, the vertical path  $X_{CO_2}$  (in ppm) can be calculated using the following equations:

$$X_{CO_2} = \frac{\tau_{CO_2}}{2 \times 10^{-6} \cdot IWF}, \quad (5)$$

$$IWF = \int_{R_G}^{R_A} \frac{N_A \cdot p(r) \cdot \Delta\sigma_{CO_2}(p(r), T(r))}{RT(r)(1 + X_{H_2O}(r))} dr, \quad (6)$$

190 where  $N_A$  is the Avogadro's constant,  $R$  is the gas constant,  $p(r)$  and  $T(r)$  are the pressure and temperature profiles, respectively.  $X_{H_2O}$  is the dry-air ratio of water vapor,  $IWF$  represents the integral weight function.  $IWF$  can be calculated using the temperature, pressure and humidity profiles obtained by the AIMMS and the High-resolution Transmission Molecular Absorption (HITRAN) database (Gordon et al., 2017).

(Zhu et al., 2020) used the Matched Filter Algorithm (MFA) to extract the weak echo signals over the ocean in a previous  
195 research work. In addition, the differences between the Pulse Peak Method (PPM) and PIM were also compared while calculating the DAOD (refer to Eq. (2)). The results showed that the SNR and accuracy of PIM were higher than those of the PPM. In this study, the PIM uses the integrated value of the points on the pulse to calculate DAOD. In our experiment, the random noise followed Gaussian distribution. When the points on the pulse are superposed, the sum continues following the Gaussian distribution of  $N(\rho^l, (\varepsilon^l)^2)$ , where the mean and the variance are (Zhu et al., 2020; Yoann et al., 2018)

$$200 \quad \rho^l = \frac{1}{N} \sum_{k=1}^N \alpha_k^l, \quad (7)$$

$$(\varepsilon^l)^2 = \frac{1}{N^2} \sum_{k=1}^N (\sigma_k^l)^2, \quad (8)$$

Where,  $N$  is the point number of the pulse,  $\rho^l$  and  $\varepsilon^l$  represent the mean and standard deviation.  $\alpha_k^l$  is the value of each point on the pulse, and  $\sigma_k^l$  is the standard deviation of each point. Hence, the empirical estimate of the SNR of the equivalent measurement on the whole averaging window can be written

$$205 \quad SNR_{PIM}^l = \frac{\rho^l}{\varepsilon^l} = \frac{\sum_{k=1}^N \alpha_k^l}{\sqrt{\sum_{k=1}^N (\sigma_k^l)^2}}, \quad (9)$$

Therefore, we can choose the number of points on the pulse to improve the SNR of each pulse.

### 3 Results and Discussion

#### 3.1 Original Echo Signals

The performance of the ACDL system was evaluated by comparing the original echo signals over three different surface types, including the ocean, the mountain, and the urban residential surface types. The original signals of the ACDL over the ocean, urban residential, and mountainous areas are shown in Figures 4, 5, and 6, respectively. Including local amplification of each signal. The amplification signals from left to right are online monitor signal, online echo signal, offline monitor signal and offline echo signal. In each group of original echo signals, the online and offline monitor signals are fixed at the same position but the echo signals appear in different positions due to the different heights of the ground surface. The original signals were filtered before using, and the signals whose pulse peak values were not in the linear region of APD were discarded. The echo signals in the ocean area were significantly smaller than those over the residential and the mountain areas. This might be due to the low reflectivity of the ocean, which leads to the reduction of the signal noise ratio (SNR) over the ocean.

#### 3.2 Data Processing and Inversion Results

We can increase the SNR of each pulse by accumulating the number of points on the pulse. Figure 7a shows the online wavelength monitoring signal, and figure 7b shows the change of SNR related to the number of accumulated points taken on the pulse. Figure 8a and 9a show the typical echo signals over the land and the ocean area. Figure 8b and 9b show the change of SNR related to the number of accumulated points taken on the pulse over different surface types. For the residential and mountain areas, the SNR was the highest when 5 points were taken before the pulse peak and 9 points were taken after the peak. And for the weak echo signal in the ocean area, when 7 points were taken before the pulse peak and 10 points were taken after the peak, the SNR was the largest.

The DAOD results calculated using the IPDA theory are shown in Figure 10. The DOAD values were smaller over the mountain area, however, no difference was found between the DAOD values of ocean and residential areas. The average DAOD values over ocean, mountainous and residential areas were 0.46, 0.44 and 0.46, respectively. The results of the IWF and the XCO<sub>2</sub> calculated using equations 5 and 6 are shown in figures 11 and 12. The average values of the IWF over ocean, mountainous and residential areas are 1083.26, 1037.05, and 1079.75, respectively. In addition, the standard deviation of the



IWF was the smallest for ocean surface and the largest for the mountainous area. The higher standard deviation for mountainous areas might be due to the fluctuations in height. Before retrieving the XCO<sub>2</sub>, the aircraft attitude angle and the doppler shift were corrected using the inertial navigation data. The XCO<sub>2</sub> calculated from the ACDL measurements is shown in Figure 12. The XCO<sub>2</sub> is the largest over residential areas and the smallest over ocean. The largest XCO<sub>2</sub> over the urban residential areas might be attributed to the strong anthropogenic emissions (Mustafa et al., 2020), and the water body is generally a sink of the CO<sub>2</sub>. The average values of XCO<sub>2</sub> over ocean, mountainous and residential areas were 421.11 ppm, 427.67 ppm, and 432.04 ppm, respectively. Correspondingly, the standard deviation of XCO<sub>2</sub> over ocean, mountainous and residential areas were 1.24, 0.58, and 0.74 (20 seconds averaged), respectively. The distribution of XCO<sub>2</sub> on the flight trajectory and the surface photos captured using the installed coloured CMOS camera are shown in Figure 13.

### 240 3.3 In-Situ Measurement Results

The XCO<sub>2</sub> measured by IPDA lidar is a distance average value, which is different from the measured value of in-situ instrument at aircraft altitude. Therefore, it is unreasonable to directly compare the two measurement results. This paper only compares the long-term change trend of XCO<sub>2</sub> measured by IPDA lidar system with the CO<sub>2</sub> volume mixing ratio measured by UGGA, which can indirectly evaluate the working performance of IPDA lidar. Figure 14 shows the comparison of the XCO<sub>2</sub> calculated from the ACDL measurements with the dry-air mole fraction of CO<sub>2</sub> measured using the UGGA. Both of the datasets show a good agreement by exhibiting a similar variation trend. The results from the two datasets also show that the volume mixing ratio of the atmospheric CO<sub>2</sub> is highest over the residential area and the lowest over ocean surface. The average value of XCO<sub>2</sub> obtained by the ACDL calculations was 426.27 ppm, and the average value of CO<sub>2</sub> mole fraction obtained by the UGGA measurements was 413.91 ppm. Moreover, the standard deviation of the UGGA observations was smaller than that of the ACDL measurements, and this might be due to the different working principles of the two instruments. The ACDL measures the weighted average concentrations at different altitudes. However, the UGGA measures the CO<sub>2</sub> value at the aircraft location.

In this study, the in-situ observations measured using the UGGA were also analysed for several days. The vertical profiles of the atmospheric CO<sub>2</sub> were measured using the UGGA during spiral and the descent of the aircraft and the results are shown in figure 15. The data recorded below 0.5 km were discarded because of sudden spikes due to slowing down of the aircraft and the associated sudden pressure changes. Figure 15 shows that the atmospheric CO<sub>2</sub> volume mixing ratio is largest near the ground, and it decreases gradually with the progression in the altitude. This might be due to the weak photosynthesis as the plants are in dormant stage during winter in northeast China (Mustafa et al., 2021). Moreover, northeast China is also a source of carbon due to heating and industrial activities, which also contributes significantly to the atmospheric CO<sub>2</sub> (Shan et al., 1997). In addition, the CO<sub>2</sub> concentration at different altitudes were the highest on 18 March. This could be caused by the weather conditions and pollution levels. Table 3 shows the weather report released by the Qinhuangdao meteorological station on each day of the flight.

**Table 3: The weather report released by the Qinhuangdao Meteorological Department on each flight day.**

Date Day Month	Weather	Temperature Highest / lowest	Wind direction/ Wind scale	AQI	PM2.5 ( $\mu\text{g}/\text{m}^3$ )	XCO <sub>2</sub> (ppm)
11 March	sunny	16°C/ -3°C	Northeast/5	80	48	416.23±2.68
14 March	sunny	14°C/ -1°C	Northeast/3	60	28	414.43±1.19
16 March	cloudy	11°C/ -1°C	North/breeze	58	30	412.82±2.14
18 March	cloudy	10°C/ 4°C	Southwest/ breeze	175	131	422.59±6.39
19 March	cloudy	15°C/ 7°C	Southeast/1	139	105	415.02±3.79

The AOD values measured using various instruments on each flight day are shown Figure 16, and the results show that the AOD was the largest on 18 March. The highest CO<sub>2</sub> concentration on March 18 was likely caused by the higher pollution levels. A ground station was arranged in the flight area to verify the airborne results. A Micro Pulse Lidar (MPL) was installed at the Funing ground station to monitor the change of local pollutants and the boundary layer. The change of pollutants and the boundary layer in Funing ground station during the flight test on March 18 is shown in Figure 17. The dry-air mole fraction of CO<sub>2</sub> reaches its maximum value at about 1.4 km on March 18 (figure 15). This might be due to the fact that the height of the boundary layer was about 1.5 km on March 18 (figure 17), and the pollutants and the greenhouse gases cannot escape through the boundary layer.

### 3.4 OCO-2 Measurement Results

During this flight experiment, the OCO-2 passed over the flight area on March 16 and the observations over the study area are shown in Figure 18. The solid red line in figure 18(a) is the flight path of the aircraft. The yellow mark point is the position of the suborbital point of the OCO-2 trajectory in the flight area. Figure 18(b) shows the XCO<sub>2</sub> results detected by OCO-2. Figure 18(c) shows the corresponding standard deviation production of OCO-2. As can be seen from Figure 18(a), OCO-2 observations covered both ocean and land surfaces. Due to the fast flight speed of the satellite, the data time period falling in the study area was from 12:57:25 to 12:57:38 UTC. A quality flag was applied to the satellite dataset and the cloud-contaminated retrievals were removed. In the flight area, there is little difference between the values of XCO<sub>2</sub> measured by OCO-2 over land and ocean areas. The average value of XCO<sub>2</sub> over land area is  $414.28 \pm 0.81$  ppm and that over ocean area is  $414.23 \pm 0.55$  ppm. However, due to the uneven distribution of CO<sub>2</sub> volume mixing ratio in the land area, the standard deviation of XCO<sub>2</sub> products over the land area is larger than that over the ocean. The XCO<sub>2</sub> measured by OCO-2 varied from 401.66 ppm to 418.80 ppm, with an average of  $414.25 \pm 0.62$  ppm.

### 3.5 Vertical Profile Comparison of CO<sub>2</sub> Concentration

The measurement results of the airborne greenhouse gas analyzer were compared with those of OCO-2 inversion and Carbon Tracker model, which is a global carbon cycle data assimilation system. The comparison results are shown in Figure 19. The

CarbonTracker dataset was interpolated to the location of the experimental site. During the flight campaigns, the OCO-2 satellite passed over the flight area on March 16. Therefore, the data results of OCO-2 on March 16 were compared with those of CarbonTracker and in-situ data on March 14, March 16 and March 19, respectively. As can be seen from the detection results in Figure 19, the structural change of CO<sub>2</sub> concentration with height can be roughly divided into two parts. From the ground to the height of 4 km and above 4 km. Below 4 km, the detection results of OCO-2, airborne greenhouse gas analyzer and CarbonTracker model show a same decreasing of CO<sub>2</sub> concentration value with the increase of altitude but the values are different. The difference between the average values of CO<sub>2</sub> concentration obtained by the OCO-2 and the airborne greenhouse gas analyzer below 4 km on March 14, March 16 and March 19 were -1.3 ppm, 0.79 ppm, and 1.3 ppm, respectively. These three methods can well detect that the land in northeast China was the source of CO<sub>2</sub> in March. This change result of airborne greenhouse gas analyzer and Carbon Tracker is more obvious than OCO-2. On March 19, CO<sub>2</sub> concentration measured by the airborne greenhouse gas analyzer decreased from 430.3 ppm at 0.34 km to 413.09 ppm at 3.18 km. The computed results of CarbonTracker decrease from 429.75 ppm at 0.59 km to 415.7 ppm at 2.68 km. The CO<sub>2</sub> concentration result of OCO-2 decreased from 414.55 ppm on the ground to 412.39 ppm at 3.02 km. When the altitude is higher than 4 km, the CO<sub>2</sub> concentration is almost constant. This might be due to the stability of the atmosphere above.

#### 300 **4 Conclusions**

In this study, a 1.57 μm double-pulse airborne IPDA LIDAR was developed for atmospheric CO<sub>2</sub> monitoring. The airborne experiment using the newly developed instrument was carried out during 11 - 19 March 2019 over Shanhaiguan, China. The IPDA LIDAR was installed on a research aircraft with some other instrument including a commercial CO<sub>2</sub> monitoring UGGA, an AIMMS, an INS, and a coloured CMOS camera. The flight path passed across various types of surfaces including the ocean, the mountain, and the residential areas. From the original signals obtained by the IPDA LIDAR, the echo signals over the ocean area were smaller than those over the mountain and the residential areas. In order to process the echo signal with low SNR over the ocean, PIM method was used to calculate DAOD. The data obtained by airborne IPDA LIDAR on March 14 was processed and analysed. The results showed that the XCO<sub>2</sub> over the ocean surface was the smallest, with an average value of  $421.11 \pm 1.24$  ppm, and that was the largest over residential area with an average value of  $432.04 \pm 0.74$  ppm. The average XCO<sub>2</sub> value over the mountainous area was  $427.67 \pm 0.58$  ppm. Moreover, the dry-air mole fraction of CO<sub>2</sub> measured by UGGA was also analysed for several days and the results showed that the CO<sub>2</sub> volume mixing ratio was largest on 18 March, that was the most polluted day during the entire flight campaign. The UGGA CO<sub>2</sub> volume mixing ratio was compared with the XCO<sub>2</sub> calculated using the IPDA LIDAR measurements, and both of the datasets showed a good agreement by exhibiting a similar variation. In addition, the vertical profiles of CO<sub>2</sub> were also measured using UGGA and compared with OCO-2 and the Carbon Tracker CO<sub>2</sub> datasets. The CO<sub>2</sub> volume mixing ratio from the Carbon Tracker was larger than the dry-air mole fraction of CO<sub>2</sub> measured using the UGGA. The atmospheric CO<sub>2</sub> volume mixing ratio was the highest near the ground and it decreased gradually with the progression in the altitude. Below 4 km, the detection results of OCO-2, airborne greenhouse gas analyzer and CarbonTracker model show a same decreasing of CO<sub>2</sub> volume mixing ratio value with the increase of altitude

but the values are different. The difference between the average values of CO<sub>2</sub> volume mixing ratio obtained by the OCO-2  
320 and the airborne greenhouse gas analyzer below 4 km on March 14, March 16 and March 19 were -1.3 ppm, 0.79 ppm, and  
1.3 ppm, respectively. These three methods can well detect that the land in northeast China was the source of CO<sub>2</sub> in March.  
This change result of airborne greenhouse gas analyzer and Carbon Tracker is more obvious than OCO-2. On March 19, CO<sub>2</sub>  
volume mixing ratio measured by the airborne greenhouse gas analyzer decreased from 430.3 ppm at 0.34 km to 413.09 ppm  
at 3.18 km. The computed results of CarbonTracker decrease from 429.75 ppm at 0.59 km to 415.7 ppm at 2.68 km. The CO<sub>2</sub>  
325 volume mixing ratio result of OCO-2 decreased from 414.55 ppm on the ground to 412.39 ppm at 3.02 km. When the altitude  
is higher than 4 km, the CO<sub>2</sub> volume mixing ratio is almost constant. This might be due to the stability of the atmosphere above.

*Author contributions.* QW and SZZ did the flight experiment, and QW processed the data results. FM provided the satellite  
and mode data and analysis methods, and FM modified the grammar and format of the whole article. LBB guided the writing  
330 of manuscripts. JQL and WBC JQL guided the flight experiment.

*Competing interests.* The authors declare that they have no conflict of interest.

*Acknowledgments.* The authors acknowledge the support of the Shanghai Institute of Satellite Engineering for conducting the  
335 experiment. The authors thank the Funing Meteorological Bureau for providing a ground station for the experiment. The  
authors acknowledge the efforts of NASA to provide the OCO-2 data products. These data were produced by the OCO-2  
project at the Jet Propulsion Laboratory, California Institute of Technology, and obtained from the OCO-2 data archive  
maintained at the NASA Goddard Earth Science Data and Information Services Center. The authors also acknowledge NOAA  
Earth System Research Laboratory for their data products. The 2nd author (Farhan Mustafa) is highly grateful to the China  
340 Scholarship Council (CSC) and the NUIST for granting the fellowship and providing the required supports.

*Financial support.* This research has been supported the National Natural Science Foundation of China (NSFC) (41675133).

## References

- Abshire, J., Ramanathan, A., Riris, H., Mao, J., Allan, G., Hasselbrack, W., Weaver, C. and Browell, E.: Airborne  
345 Measurements of CO<sub>2</sub> Column Concentration and Range Using a Pulsed Direct-Detection IPDA Lidar, *Remote Sens.*, 6(1),  
443–469, doi:10.3390/rs6010443, 2013.
- Abshire, J. B., Ramanathan, A. K., Riris, H., Allan, G. R., Sun, X., Hasselbrack, W. E., Mao, J., Wu, S., Chen, J., Numata, K.,  
Kawa, S. R., Yang, M. Y. M. and DiGangi, J.: Airborne measurements of CO<sub>2</sub> and column concentrations made with a pulsed  
IPDA lidar using a multiple-wavelength-locked laser and HgCdTe APD detector, *Atmos. Meas. Tech.*, 11(4), 2001–2025,  
350 doi:10.5194/amt-11-2001-2018, 2018.

- Amediek, A., Ehret, G., Fix, A., Wirth, M., Büdenbender, C., Quatrevalet, M., Kiemle, C. and Gerbig, C.: CHARM-F—a new airborne integrated-path differential-absorption lidar for carbon dioxide and methane observations: measurement performance and quantification of strong point source emissions, *Appl. Opt.*, 56(18), 5182, doi:10.1364/AO.56.005182, 2017.
- 355 Araki, M., Morino, I., MacHida, T., Sawa, Y., Matsueda, H., Ohyama, H., Yokota, T. and Uchino, O.: CO<sub>2</sub> column-averaged volume mixing ratio derived over Tsukuba from measurements by commercial airlines, *Atmos. Chem. Phys.*, 10(16), 7659–7667, doi:10.5194/acp-10-7659-2010, 2010.
- Babenhauserheide, A., Basu, S., Houweling, S., Peters, W. and Butz, A.: Comparing the CarbonTracker and TM5-4DVar data assimilation systems for CO<sub>2</sub> surface flux inversions, , 9747–9763, doi:10.5194/acp-15-9747-2015, 2015.
- Baer, D. S., Paul, J. B., Gupta, M. and O’Keefe, A.: Sensitive absorption measurements in the near-infrared region using off-axis integrated-cavity-output spectroscopy, *Appl. Phys. B*, 75(2), 261–265, doi:10.1007/s00340-002-0971-z, 2002.
- 360 Ballantyne, A. P., Alden, C. B., Miller, J. B., Trans, P. P. and White, J. W. C.: Increase in observed net carbon dioxide uptake by land and oceans during the past 50 years, *Nature*, 488(7409), 70–73, doi:10.1038/nature11299, 2012.
- Crisp, D.: Measuring atmospheric carbon dioxide from space with the Orbiting Carbon Observatory-2 (OCO-2), in *Proc.SPIE*, vol. 9607., 2015.
- 365 Crisp, D., Miller, C. E. and DeCola, P. L.: NASA Orbiting Carbon Observatory: measuring the column averaged carbon dioxide mole fraction from space, *J. Appl. Remote Sens.*, 2(1), 1–14, doi:10.1117/1.2898457, 2008.
- Crisp, D., Fisher, B. M., O’Dell, C., Frankenberg, C., Basilio, R., Bösch, H., Brown, L. R., Castano, R., Connor, B., Deutscher, N. M., Eldering, A., Griffith, D., Gunson, M., Kuze, A., Mandrake, L., McDuffie, J., Messerschmidt, J., Miller, C. E., Morino, I., Natraj, V., Notholt, J., O’Brien, D. M., Oyafuso, F., Polonsky, I., Robinson, J., Salawitch, R., Sherlock, V., Smyth, M.,
- 370 Suto, H., Taylor, T. E., Thompson, D. R., Wennberg, P. O., Wunch, D. and Yung, Y. L.: The ACOS CO<sub>2</sub> retrieval algorithm - Part II: Global XCO<sub>2</sub> data characterization, *Atmos. Meas. Tech.*, 5(4), 687–707, doi:10.5194/amt-5-687-2012, 2012.
- Dlugokencky Ed, T. P.: Trends in Atmospheric Carbon Dioxide, Noaa/Esrl, <http://www.esrl.noaa.gov/gmd/ccgg/trends/global.ht> [online] Available from: [ftp://aftp.cmdl.noaa.gov/products/trends/co2/co2\\_mm\\_gl.txt](ftp://aftp.cmdl.noaa.gov/products/trends/co2/co2_mm_gl.txt) (Accessed 3 May 2020), 2016.
- 375 Du, J., Zhu, Y., Li, S., Zhang, J., Sun, Y., Zang, H., Liu, D., Ma, X., Bi, D., Liu, J., Zhu, X. and Chen, W.: Double-pulse 157 μm integrated path differential absorption lidar ground validation for atmospheric carbon dioxide measurement, *Appl. Opt.*, 56(25), 7053, doi:10.1364/AO.56.007053, 2017.
- Ehret, G., Kiemle, C., Wirth, M., Amediek, A., Fix, A. and Houweling, S.: Space-borne remote sensing of CO<sub>2</sub>, CH<sub>4</sub>, and N<sub>2</sub>O by integrated path differential absorption lidar: a sensitivity analysis, *Appl. Phys. B*, 90(3–4), 593–608, doi:10.1007/s00340-007-2892-3, 2008.
- 380 Gong, Y., Bu, L., Yang, B. and Mustafa, F.: High Repetition Rate Mid-Infrared Differential Absorption Lidar for Atmospheric Pollution Detection, *Sensors*, 20(8), 2211, doi:10.3390/s20082211, 2020.
- Gordon, I. E., Rothman, L. S., Hill, C., Kochanov, R. V., Tan, Y., Bernath, P. F., Birk, M., Boudon, V., Campargue, A., Chance, K. V., Drouin, B. J., Flaud, J.-M., Gamache, R. R., Hodges, J. T., Jacquemart, D., Perevalov, V. I., Perrin, A., Shine, K. P.,

- 385 Smith, M.-A. H., Tennyson, J., Toon, G. C., Tran, H., Tyuterev, V. G., Barbe, A., Császár, A. G., Devi, V. M., Furtenbacher, T., Harrison, J. J., Hartmann, J.-M., Jolly, A., Johnson, T. J., Karman, T., Kleiner, I., Kyuberis, A. A., Loos, J., Lyulin, O. M., Massie, S. T., Mikhailenko, S. N., Moazzen-Ahmadi, N., Müller, H. S. P., Naumenko, O. V., Nikitin, A. V., Polyansky, O. L., Rey, M., Rotger, M., Sharpe, S. W., Sung, K., Starikova, E., Tashkun, S. A., Auwera, J. Vander, Wagner, G., Wilzewski, J., Wcisło, P., Yu, S. and Zak, E. J.: The HITRAN2016 molecular spectroscopic database, *J. Quant. Spectrosc. Radiat. Transf.*,  
390 203, 3–69, doi:10.1016/j.jqsrt.2017.06.038, 2017.
- Hedelius, J. K., Parker, H., Wunch, D., Roehl, C. M., Viatte, C., Newman, S., Toon, G. C., Podolske, J. R., Hillyard, P. W., Iraci, L. T., Dubey, M. K. and Wennberg, P. O.: Intercomparability of XCO<sub>2</sub> and XCH<sub>4</sub> from the United States TCCON sites, *Atmos. Meas. Tech.*, 10(4), 1481–1493, doi:10.5194/amt-10-1481-2017, 2017.
- Hungershoefer, K., Peylin, P., Chevallier, F., Rayner, P., Klonecki, A., Houweling, S. and Marshall, J.: Evaluation of various  
395 observing systems for the global monitoring of CO<sub>2</sub> surface fluxes, *Atmos. Chem. Phys.*, 10(21), 10503–10520, doi:10.5194/acp-10-10503-2010, 2010.
- Jacobson, A. R., Schuldt, K. N., Miller, J. B., Tans, P., Andrews, A., Mund, J., Aalto, T., Bakwin, P., Bergamaschi, P., Biraud, S. C., Chen, H., Colomb, A., Conil, S., Cristofanelli, P., Davis, K., Delmotte, M., DiGangi, J. P., Dlugokencky, E., Emmenegger, L., Fischer, M. L., Hatakka, J., Heliasz, M., Hermanssen, O., Holst, J., Jaffe, D., Karion, A., Keronen, P.,  
400 Kominkova, K., Kubistin, D., Laurent, O., Laurila, T., Lee, J., Lehner, I., Leuenberger, M., Lindauer, M., Löffvenius, M. O., Lopez, M., Mammarella, I., Manca, G., Marek, M. V., Marklund, P., Martin, M. Y., McKain, K., Miller, C. E., Mölder, M., Myhre, C. L., Pichon, J. M., Plass-Dölmer, C., Ramonet, M., Scheeren, B., Schumacher, M., Sloop, C. D., Steinbacher, M., Sweeney, C., Thoning, K., Tørseth, K., Turnbull, J., Viner, B., Vitkova, G., Wekker, S. De, Weyrauch, D. and Worthy, D.: CarbonTracker Near Real-Time, CT-NRT.v2020-1, , doi:10.25925/RCHH-MS75, 2020.
- 405 Kawa, S. R., Mao, J., Abshire, J. B., Collatz, G. J., Sun, X. and Weaver, C. J.: Simulation studies for a space-based CO<sub>2</sub> lidar mission, *Tellus B Chem. Phys. Meteorol.*, 62(5), 759–769, doi:10.1111/j.1600-0889.2010.00486.x, 2010.
- Kiel, M., Dell, C. W. O., Fisher, B., Eldering, A., Nassar, R., Macdonald, C. G. and Wennberg, P. O.: How bias correction goes wrong : measurement of X CO<sub>2</sub> affected by erroneous surface pressure estimates, , 2241–2259, 2019.
- Kong, Y., Chen, B. and Measho, S.: Spatio-temporal consistency evaluation of XCO<sub>2</sub> retrievals from GOSAT and OCO-2  
410 based on TCCON and model data for joint utilization in carbon cycle research, *Atmosphere (Basel)*, 10(7), 1–23, doi:10.3390/atmos10070354, 2019.
- Krol, M. C., S. Houweling, B. Bregman, M. van den Broek, A. Segers, P. van Velthoven, W. Peters, F. J. Dentener, and P. Bergamaschi (2005), The two-way nested global chemistry-transport zoom model TM5: Algorithm and applications, *Atmos. Chem. Phys.*, 5, 417– 432.
- 415 Kulawik, S., Wunch, D., Dell, C. O., Frankenberg, C., Reuter, M., Oda, T., Chevallier, F., Sherlock, V., Buchwitz, M., Osterman, G., Miller, C. E., Wennberg, P. O., Griffith, D., Morino, I., Dubey, M. K., Deutscher, N. M., Notholt, J., Hase, F., Warneke, T., Sussmann, R., Robinson, J., Strong, K., Schneider, M., Mazière, M. De, Shiomi, K., Feist, D. G., Iraci, L. T., Wolf, J., Environm, A. and Inst, R.: Consistent evaluation of ACOS-GOSAT , BESD-SCIAMACHY , CarbonTracker , and

- MACC through comparisons to TCCON, , 683–709, doi:10.5194/amt-9-683-2016, 2016.
- 420 Lei, L., Zhong, H., He, Z., Cai, B., Yang, S., Wu, C., Zeng, Z., Liu, L. and Zhang, B.: Assessment of atmospheric CO<sub>2</sub> concentration enhancement from anthropogenic emissions based on satellite observations, *Kexue Tongbao/Chinese Sci. Bull.*, 62(25), 2941–2950, doi:10.1360/N972016-01316, 2017.
- Liang, A., Gong, W., Han, G. and Xiang, C.: Comparison of satellite-observed XCO<sub>2</sub> from GOSAT, OCO-2, and ground-based TCCON, *Remote Sens.*, 9(10), 1–26, doi:10.3390/rs9101033, 2017.
- 425 Lindqvist, H., O’Dell, C. W., Basu, S., Boesch, H., Chevallier, F., Deutscher, N., Feng, L., Fisher, B., Hase, F., Inoue, M., Kivi, R., Morino, I., Palmer, P. I., Parker, R., Schneider, M., Sussmann, R. and Yoshida, Y.: Does GOSAT capture the true seasonal cycle of carbon dioxide?, *Atmos. Chem. Phys.*, 15(22), 13023–13040, doi:10.5194/acp-15-13023-2015, 2015.
- Mao, J., Ramanathan, A., Abshire, J. B., Kawa, S. R., Riris, H., Allan, G. R., Rodriguez, M., Hasselbrack, W. E., Sun, X., Numata, K., Chen, J., Choi, Y. and Yang, M. Y. M.: Airborne lidar reflectance measurements at 1.57  $\mu$  m in support of the
- 430 A-SCOPE mission for atmospheric CO<sub>2</sub>, *Atmos. Meas. Tech.*, 11(1), 127–140, doi:10.5194/amt-11-127-2018, 2018a.
- Mao, J., Ramanathan, A., Abshire, J. B., Kawa, S. R., Riris, H., Allan, G. R., Rodriguez, M., Hasselbrack, W. E., Sun, X., Numata, K., Chen, J., Choi, Y. and Yang, M. Y. M.: Measurement of atmospheric CO<sub>2</sub> column concentrations to cloud tops with a pulsed multi-wavelength airborne lidar, *Atmos. Meas. Tech.*, 11(1), 127–140, doi:10.5194/amt-11-127-2018, 2018b.
- Mendonca, J., Strong, K., Wunch, D., Toon, G. C., Long, D. A., Hodges, J. T., Sironneau, V. T. and Franklin, J. E.: Using a
- 435 speed-dependent Voigt line shape to retrieve O<sub>2</sub> from Total Carbon Column Observing Network solar spectra to improve measurements of XCO<sub>2</sub>, *Atmos. Meas. Tech.*, 12(1), 35–50, doi:10.5194/amt-12-35-2019, 2019.
- Mustafa, F., Bu, L., Wang, Q., Ali, M. A., Bilal, M., Shahzaman, M. and Qiu, Z.: Multi-year comparison of CO<sub>2</sub> concentration from NOAA carbon tracker reanalysis model with data from GOSAT and OCO-2 over Asia, *Remote Sens.*, 12(15), doi:10.3390/RS12152498, 2020.
- 440 Mustafa, F., Wang, H., Bu, L., Wang, Q., Shahzaman, M., Bilal, M., Zhou, M., Iqbal, R., Aslam, R. W., Ali, M. A. and Qiu, Z.: Validation of GOSAT and OCO-2 against In Situ Aircraft Measurements and Comparison with CarbonTracker and GEOS-Chem over Qinhuaodao, China, *Remote Sens.*, 13(5), 899, doi:10.3390/rs13050899, 2021.
- O’Dell, C. W., Connor, B., Bösch, H., O’Brien, D., Frankenberg, C., Castano, R., Christi, M., Eldering, D., Fisher, B., Gunson, M., McDuffie, J., Miller, C. E., Natraj, V., Oyafuso, F., Polonsky, I., Smyth, M., Taylor, T., Toon, G. C., Wennberg, P. O. and
- 445 Wunch, D.: The ACOS CO<sub>2</sub> retrieval algorithm-Part 1: Description and validation against synthetic observations, *Atmos. Meas. Tech.*, 5(1), 99–121, doi:10.5194/amt-5-99-2012, 2012.
- Paul, J. B., Lapson, L. and Anderson, J. G.: Ultrasensitive absorption spectroscopy with a high-finesse optical cavity and off-axis alignment, *Appl. Opt.*, 40(27), 4904–4910, doi:10.1364/AO.40.004904, 2001.
- W. Peters, M. C. Krol, E. J. Dlugokencky, F. J. Dentener, P. Bergamaschi, G. Dutton, P. v. Velthoven, J. B. Miller, L. Bruhwiler,
- 450 and P. P. Tan, Toward regional-scale modeling using the two-way nested global model TM5: Characterization of transport using SF<sub>6</sub>, *J. Geophys. Res.*, 109, D19314, doi:10.1029/2004JD005020, 2004.
- Refaat, T. F., Singh, U. N., Yu, J., Petros, M., Ismail, S., Kavaya, M. J. and Davis, K. J.: Evaluation of an airborne triple-

- pulsed 2  $\mu\text{m}$  IPDA lidar for simultaneous and independent atmospheric water vapor and carbon dioxide measurements, *Appl. Opt.*, 54(6), 1387, doi:10.1364/AO.54.001387, 2015.
- 455 Refaat, T. F., Singh, U. N., Yu, J., Petros, M., Remus, R. and Ismail, S.: Double-pulse 2- $\mu\text{m}$  integrated path differential absorption lidar airborne validation for atmospheric carbon dioxide measurement, *Appl. Opt.*, 55(15), 4232, doi:10.1364/AO.55.004232, 2016.
- Santer, B. D., Painter, J. F., Bonfils, C., Mears, C. A., Solomon, S., Wigley, T. M. L., Gleckler, P. J., Schmidt, G. A., Doutriaux, C., Gillett, N. P., Taylor, K. E., Thorne, P. W. and Wentz, F. J.: Human and natural influences on the changing thermal structure of the atmosphere, *Proc. Natl. Acad. Sci. U. S. A.*, 110(43), 17235–17240, doi:10.1073/pnas.1305332110, 2013.
- 460 Schultz, M. G., Akimoto, H., Bottenheim, J., Buchmann, B., Galbally, I. E., Gilge, S., Helmig, D., Koide, H., Lewis, A. C., Novelli, P. C., Plass-Dölmer, C., Ryerson, T. B., Steinbacher, M., Steinbrecher, R., Tarasova, O., Tørseth, K., Thouret, V. and Zellweger, C.: The global atmosphere watch reactive gases measurement network, *Elementa*, 3, 1–23, doi:10.12952/journal.elementa.000067, 2015.
- 465 Shan, Y., Guan, D., Zheng, H., Ou, J., Li, Y., Meng, J., Mi, Z., Liu, Z. and Zhang, Q.: China CO<sub>2</sub> emission accounts 1997–2015, *Sci. Data*, 1–14 [online] Available from: [www.nature.com/sdata/](http://www.nature.com/sdata/), 1997.
- Stocker, B. D., Roth, R., Joos, F., Spahni, R., Steinacher, M., Zaehle, S., Bouwman, L., Xu-Ri and Prentice, I. C.: Multiple greenhouse-gas feedbacks from the land biosphere under future climate change scenarios, *Nat. Clim. Chang.*, 3(7), 666–672, doi:10.1038/nclimate1864, 2013.
- 470 Sun, X., Duan, M., Gao, Y., Han, R., Ji, D., Zhang, W., Chen, N., Xia, X., Liu, H. and Huo, Y.: In situ measurement of CO<sub>2</sub> and CH<sub>4</sub> from aircraft over northeast China and comparison with OCO-2 data, *Atmos. Meas. Tech.*, 13(7), 3595–3607, doi:10.5194/amt-13-3595-2020, 2020.
- UNFCCC: Paris Agreement., 2015.
- Wunch, D., Wennberg, P. O., Osterman, G., Fisher, B., Naylor, B., Roehl, M. C., O'Dell, C., Mandrake, L., Viatte, C., Kiel, M., Griffith, D. W. T., Deutscher, N. M., Velazco, V. A., Notholt, J., Warneke, T., Petri, C., De Maziere, M., Sha, M. K., Sussmann, R., Rettinger, M., Pollard, D., Robinson, J., Morino, I., Uchino, O., Hase, F., Blumenstock, T., Feist, D. G., Arnold, S. G., Strong, K., Mendonca, J., Kivi, R., Heikkinen, P., Iraci, L., Podolske, J., Hillyard, P., Kawakami, S., Dubey, M. K., Parker, H. A., Sepulveda, E., García, O. E., Te, Y., Jeseck, P., Gunson, M. R., Crisp, D. and Eldering, A.: Comparisons of the Orbiting Carbon Observatory-2 (OCO-2) XCO<sub>2</sub> measurements with TCCON, *Atmos. Meas. Tech.*, 10(6), 2209–2238, doi:10.5194/amt-10-2209-2017, 2017.
- 480 Xie, J., Huang, X., Bu, L., Zhang, H., Mustafa, F. and Chu, C.: Detection of water cloud microphysical properties using multi-scattering polarization lidar, *Curr. Opt. Photonics*, 4(3), 174–185, doi:10.3807/COPP.2020.4.3.174, 2020.
- Yang, S., Lei, L., Zeng, Z., He, Z. and Zhong, H.: An Assessment of Anthropogenic CO<sub>2</sub> Emissions by Satellite-Based Observations in China, *Sensors (Basel)*, 19(5), 1118, doi:10.3390/s19051118, 2019.
- 485 Yokota, T., Yoshida, Y., Eguchi, N., Ota, Y., Tanaka, T., Watanabe, H. and Maksyutov, S.: Global Concentrations of CO<sub>2</sub> and CH<sub>4</sub> Retrieved from GOSAT : First Preliminary Results, , 5, 160–163, 2009.

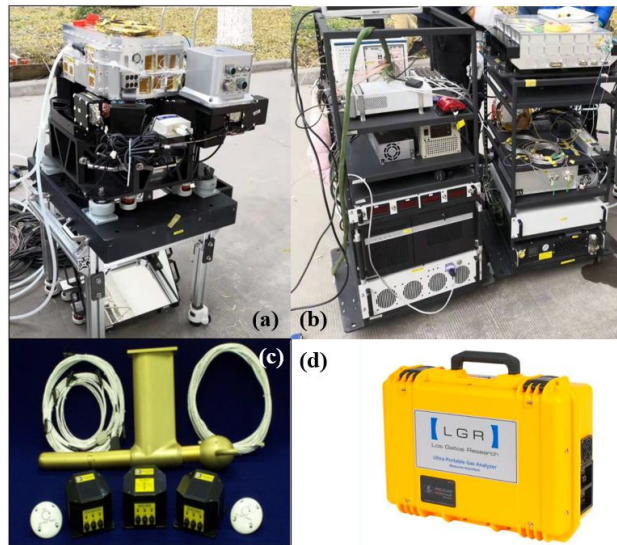


Yu, J., Petros, M., Singh, U. N., Refaat, T. F., Reithmaier, K., Remus, R. G. and Johnson, W.: An Airborne 2- $\mu\text{m}$  Double-Pulsed Direct-Detection Lidar Instrument for Atmospheric CO<sub>2</sub> Column Measurements, *J. Atmos. Ocean. Technol.*, 34(2), 385–400, doi:10.1175/JTECH-D-16-0112.1, 2017.

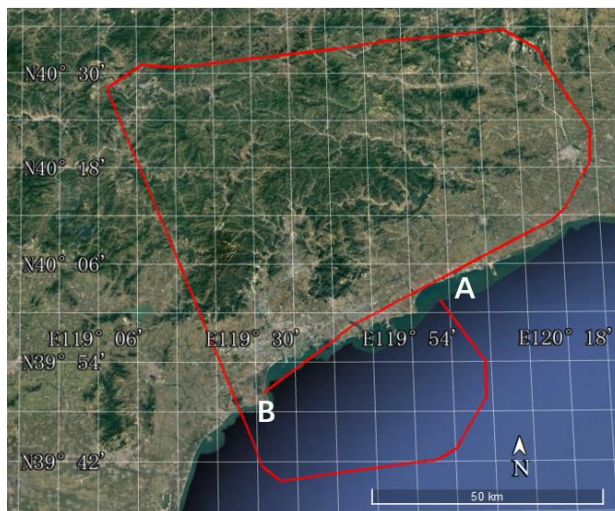
490 Zhang, X., Wang, F., Wang, W., Huang, F., Chen, B., Gao, L., Wang, S., Yan, H., Ye, H., Si, F., Hong, J., Li, X., Cao, Q., Che, H. and Li, Z.: The development and application of satellite remote sensing for atmospheric compositions in China, *Atmos. Res.*, 245, 105056, doi:10.1016/j.atmosres.2020.105056, 2020.

Zhu, Y., Yang, J., Chen, X., Zhu, X., Zhang, J., Li, S., Sun, Y., Hou, X., Bi, D., Bu, L., Zhang, Y., Liu, J. and Chen, W.: Airborne Validation Experiment of 1.57- $\mu\text{m}$  Double-Pulse IPDA LIDAR for Atmospheric Carbon Dioxide Measurement, *Remote Sens.*, 12(12), 1999, doi:10.3390/rs12121999, 2020.

495 Yoann, T., P, Clémence., Martin, W., Fabien, G., Fabien, M.: Averaging Bias Correction for Future IPDA Lidar Mission MERLIN. *Atmos. Meas. Tech.*, 11, 5865–5884, 2018

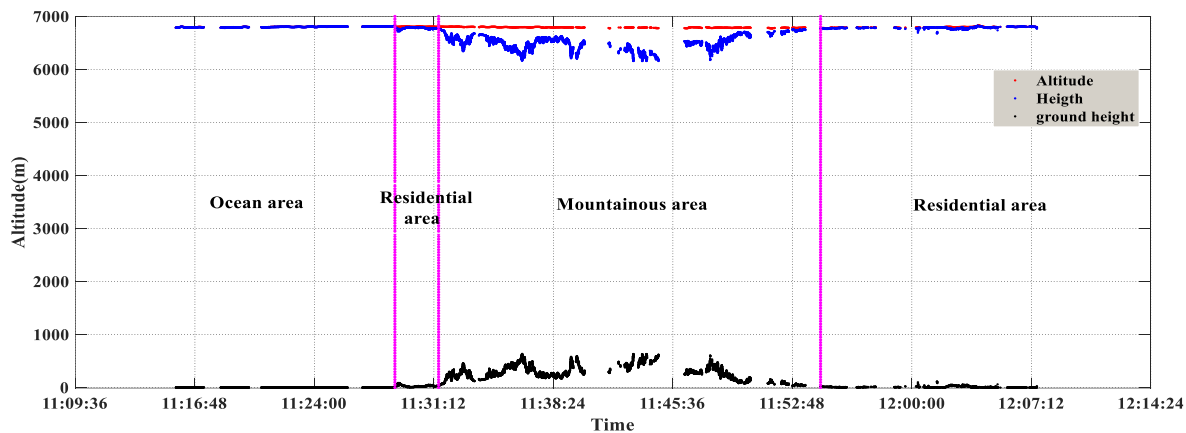


500 **Figure 1: The physical picture of IPDA lidar system. (a) It is the transceiver system, installed in the pod outside the aircraft. (b) It is the control system and data acquisition system of some equipment, which is installed in the sealed cabin of the aircraft. (c) It is the the Aircraft Integrated Meteorological Measurement System (AIMMS). (d) It is a commercial instrument Ultraportable Greenhouse Gas Analyzer, that was installed in an unsealed cabin of the aircraft.**

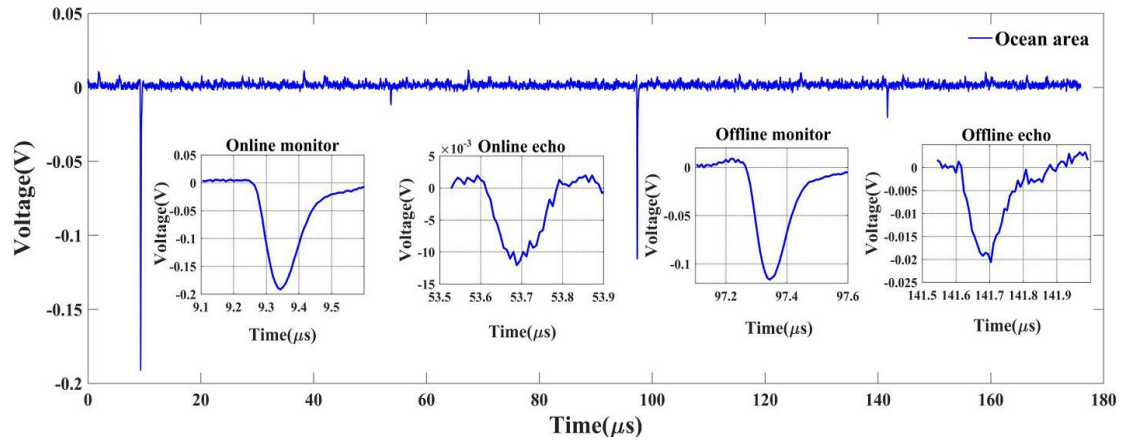


505

Figure 2: Flight trajectory of the flight on 14 March 2019. The starting point of the flight was A, and the ending point was B (© Google Earth Pro).

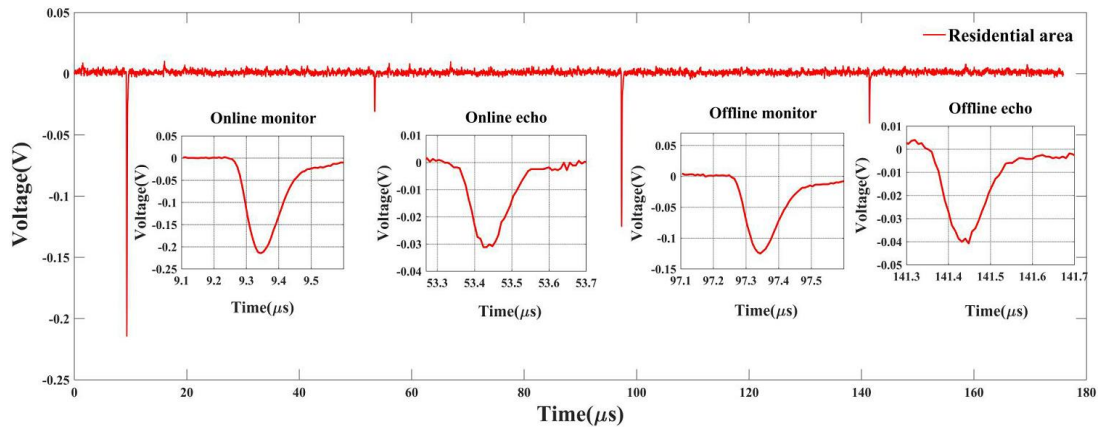


510 Figure 3: Aircraft flight height and corresponding surface elevation on 14 March 2019. The red dots are the altitude of the aircraft measured by the onboard GPS system. The blue scatter points are the distance between the plane and ground measured by lidar. The black scattered points are the difference between the altitude measured by the GPS and the distance measured by the lidar, and also represent the surface elevation. The purple-red vertical line is the dividing line for different surface types.



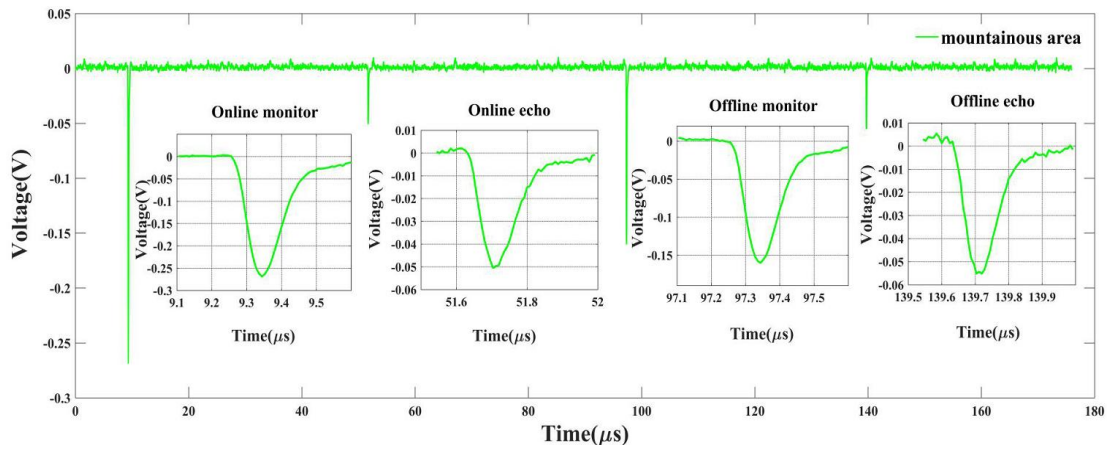
515

Figure 4: Original echo signal of ocean area (total signal and pulse amplification signal). The amplification signals from left to right are online monitor signal, online echo signal, offline monitor signal and offline echo signal.



520

Figure 5: Original echo signal of urban residential area (total signal and pulse amplification signal). The amplification signals from left to right are online monitor signal, online echo signal, offline monitor signal and offline echo signal.



525 **Figure 6:** Original echo signal of mountainous area (total signal and pulse amplification signal). The amplification signals from left to right are online monitor signal, online echo signal, offline monitor signal and offline echo signal.

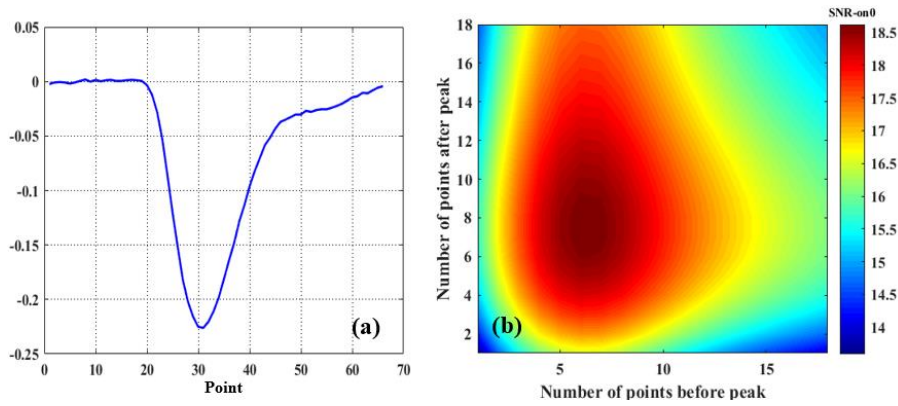
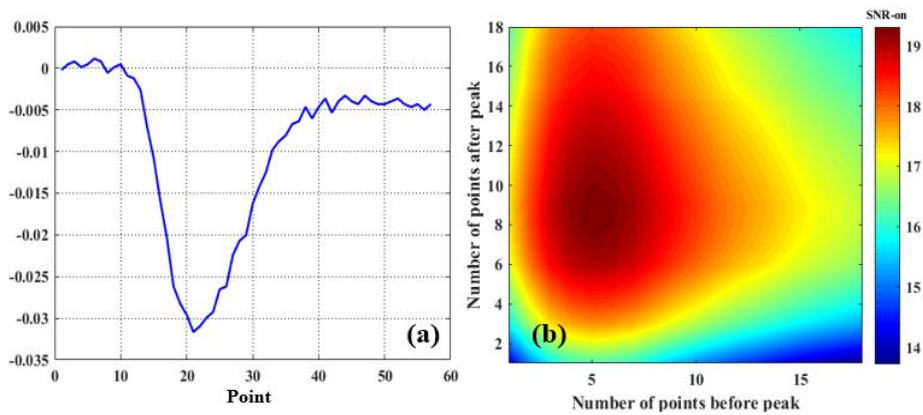
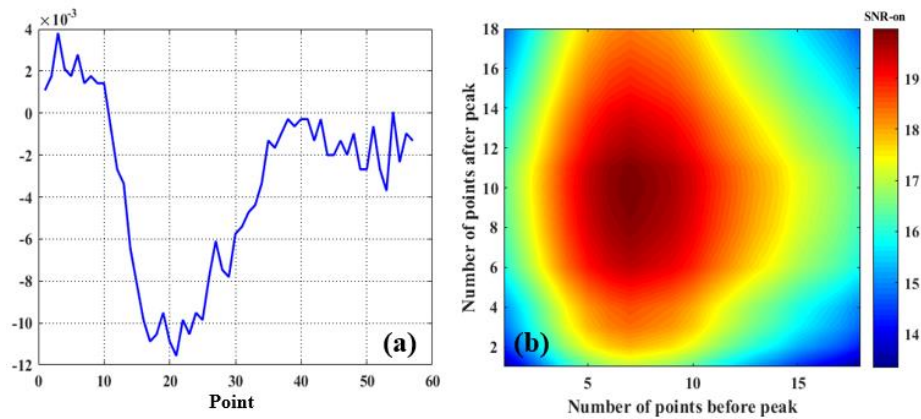


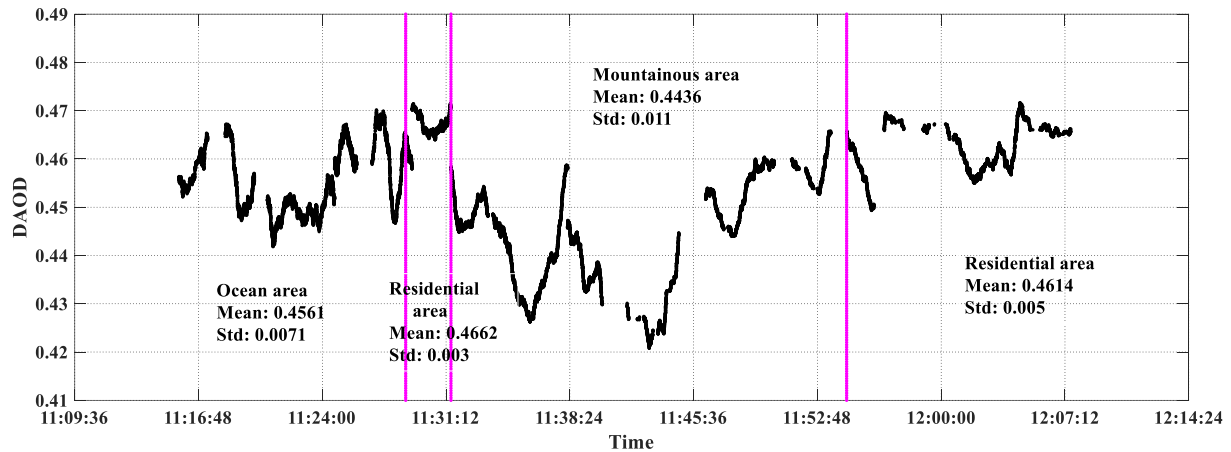
**Figure 7:** (a) Online wavelength monitoring pulse signal. (b) The change of pulse signal SNR with the number of selected pulse points.



530 **Figure 8:** (a) Online wavelength echo pulse signal in land area. (b) The change of the SNR of the echo pulse signal in the land area with the number of selected pulse points.



535 **Figure 9: (a) Online wavelength echo pulse signal in ocean area. (b) The change of the SNR of the echo pulse signal in the ocean area with the number of selected pulse points.**



540 **Figure 10: DAOD results over ocean areas, urban residential areas and mountain areas on 14 March 2019. The purplish red vertical line represents the boundary of different surface types. The plane passes through the ocean area, urban residential area, mountain area and urban residential area in turn, which is the same in the following results.**

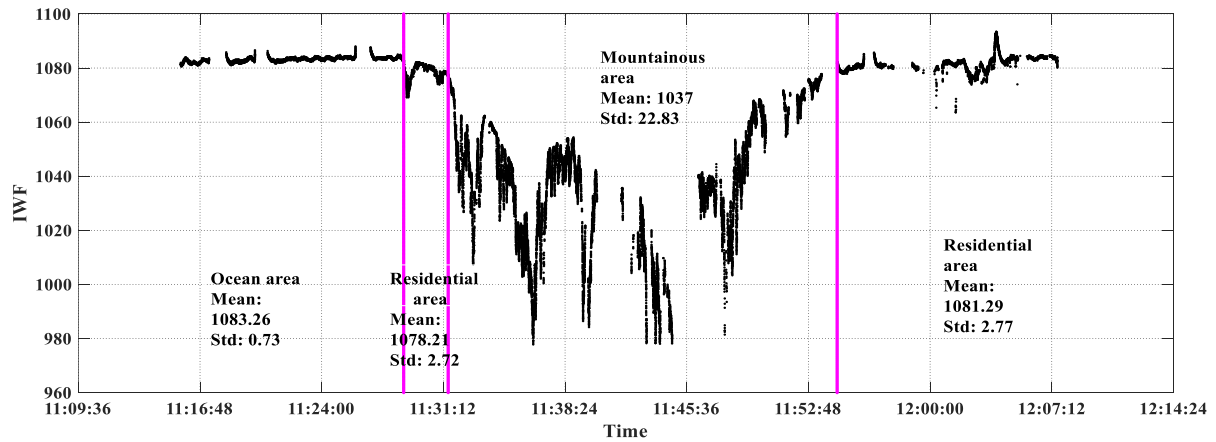
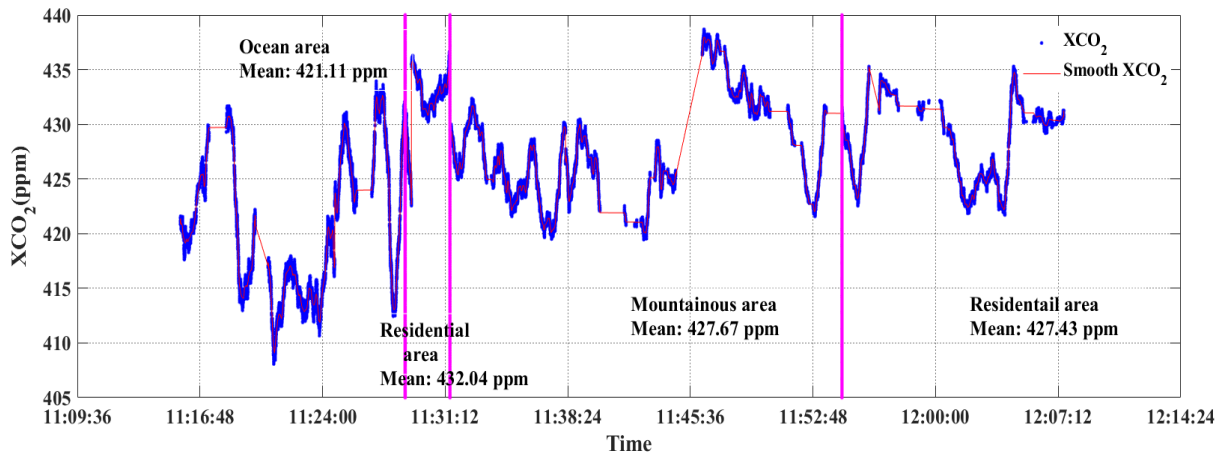
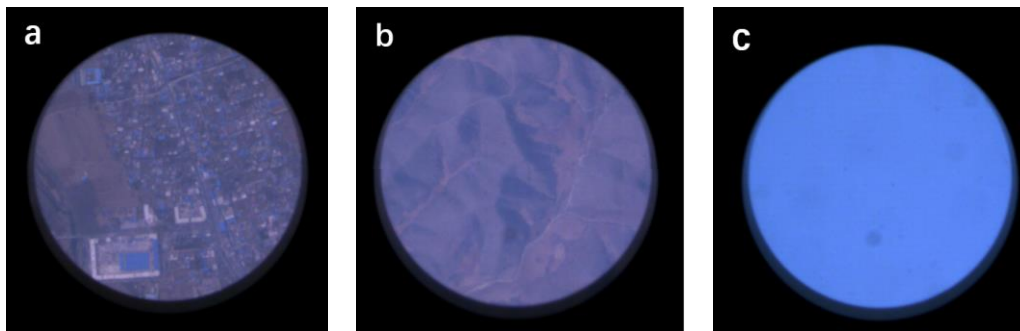
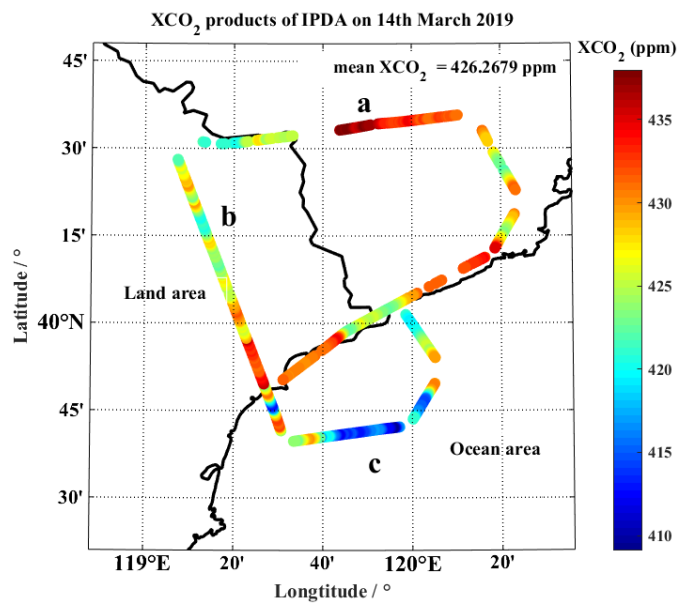


Figure 11: IWF results over ocean, urban residential and mountainous areas on 14 March 2019. The purplish red vertical line represents the boundary of different surface types.

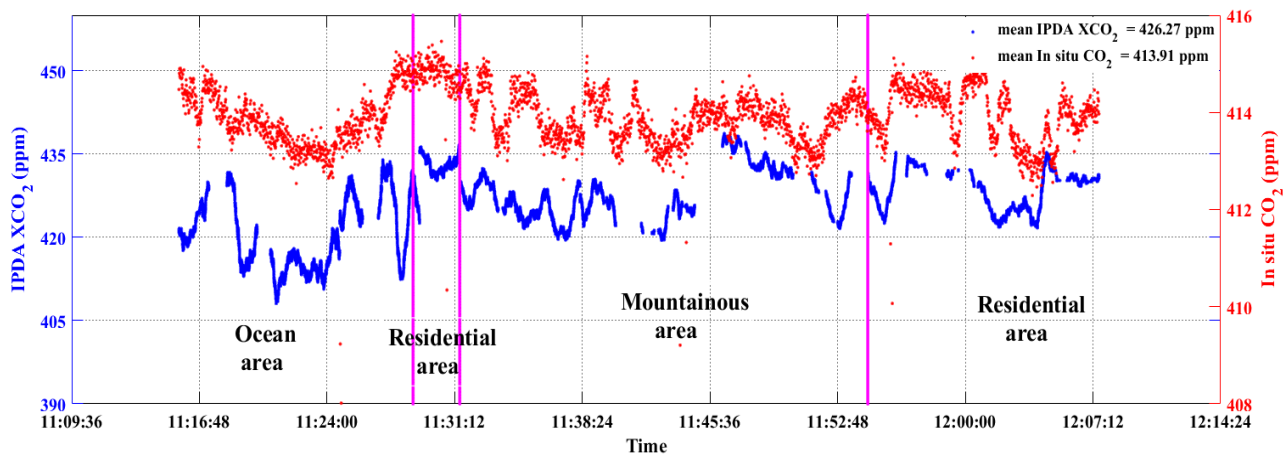


545 Figure 12: XCO<sub>2</sub> results over ocean, urban residential and mountainous areas on 14 March 2019. The purplish red vertical line represents the boundary of different surface types.





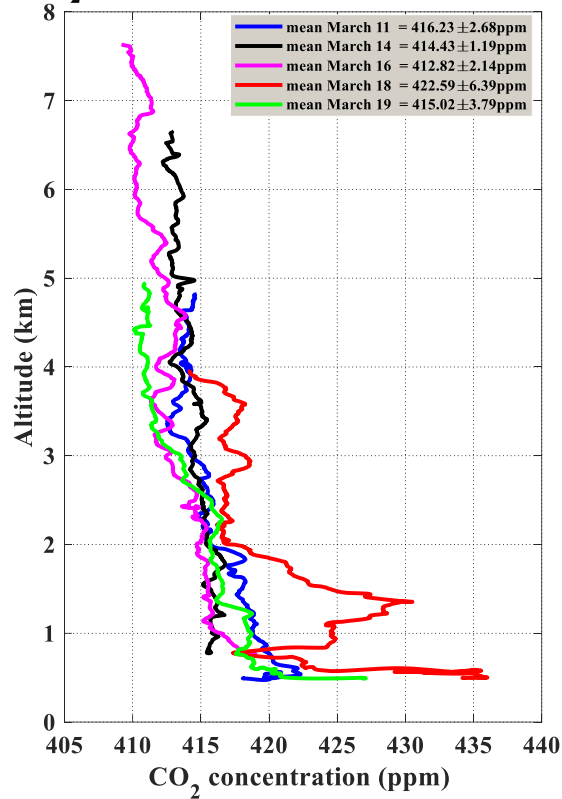
550 Figure 13: XCO<sub>2</sub> distribution on the flight trajectory and surface photos of typical areas on 14 March 2019. Among them, a represents the urban residential area, b represents the mountain area, and c represents the ocean area.



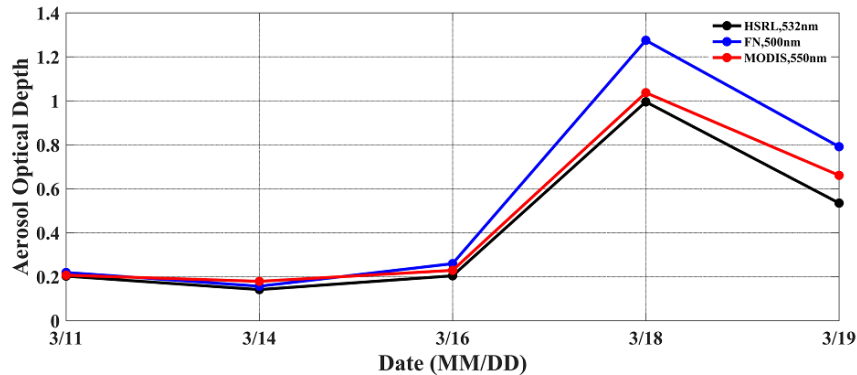
555 **Figure 14: XCO<sub>2</sub> comparison results of airborne IPDA lidar and LGR on 14 March 2019. The red scatter is the result of greenhouse gas analyzer. The blue scatter is measured by airborne IPDA lidar. The purplish red vertical line represents the boundary of different surface types. The plane passes through the ocean area, urban residential area, mountain area and urban residential area in turn.**



CO<sub>2</sub> Concentration profile measured by LGR



560 Figure 15: CO<sub>2</sub> concentration profile results measured by greenhouse gas analyzer during aircraft descending flight on different dates. The blue solid line is the result on March 11. The black solid line is the result of March 14. The purple solid line is the result of March 16. The solid red line is the result of March 18. The green solid line is the result of March 19.



565 Figure 16: Aerosol optical depth results on different dates. The blue scatters are measured by the sun photometer of Funing ground station. The black scatters are the measurement results of the airborne lidar 532nm channel. The red scatters are the measurement results of Moderate Resolution Imaging Spectroradiometer (MODIS).

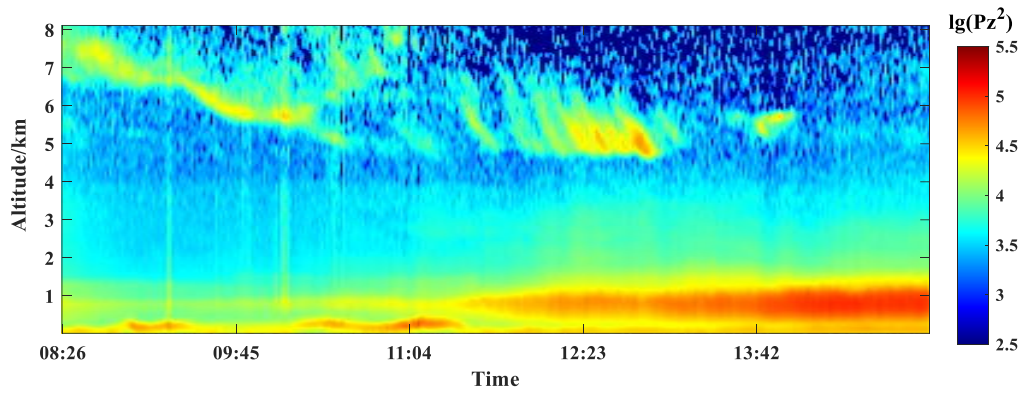
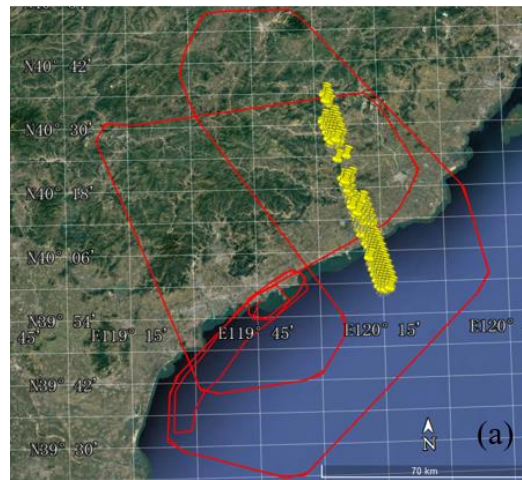
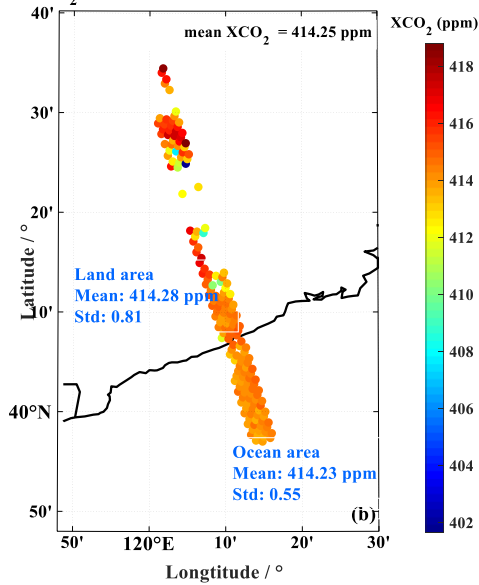


Figure 17: MPL measurement results of Funing ground station on March 18.



570

$\text{XCO}_2$  products of OCO-2 on 16th March 2019



$\text{XCO}_2$  std products of OCO-2 on 16th March 2019

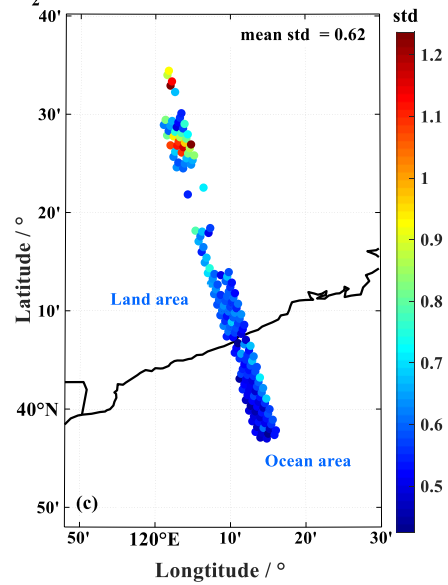


Figure 18: Orbit and detection results of OCO-2 satellite on March 16. The solid red line in figure (a) is the flight path of the aircraft. The yellow mark point is the position of the suborbital point of the OCO-2 trajectory in the flight area (© Google Earth Pro). Figure (b) shows the XCO<sub>2</sub> results detected by OCO-2. Figure (c) shows the corresponding standard deviation.

575

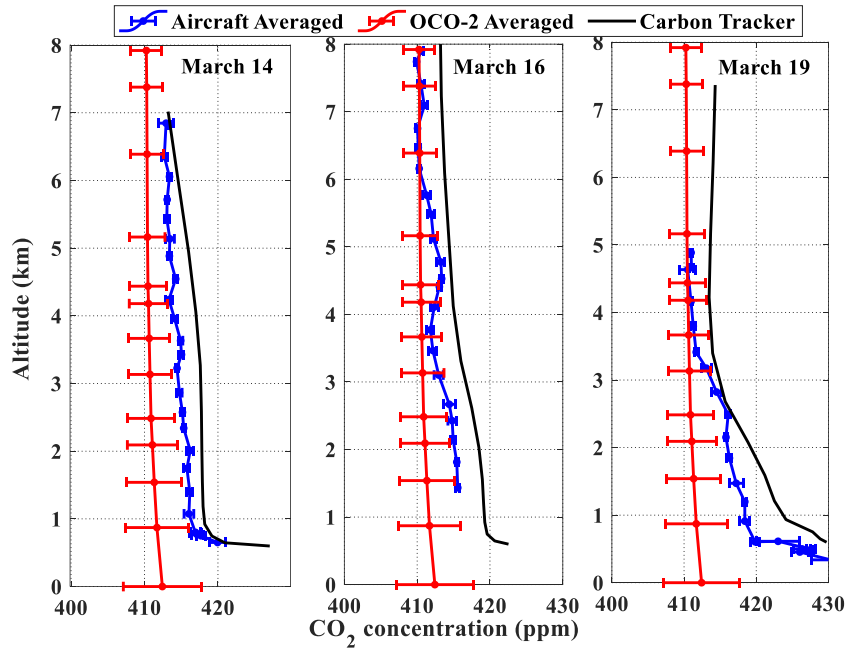


Figure 19: CO<sub>2</sub> volume mixing ratio profile comparison results of airborne greenhouse gas analyzer and OCO-2 satellite, CT model. Figure (a) is the vertical structure of CO<sub>2</sub> volume mixing ratio on March 14. Figure (b) shows the vertical structure of CO<sub>2</sub> volume mixing ratio on March 16. Figure (c) shows the vertical structure of CO<sub>2</sub> volume mixing ratio on March 19. The red errorbars is the inversion result of OCO-2. The blue errorbars is the measurement result of the airborne greenhouse gas analyzer. The black solid line is the result of CT model.

580